ADVANCED MATERIALS

www.advmat.de

Critical Role of Interface and Crystallinity on the Performance and Photostability of Perovskite Solar Cell on Nickel Oxide

Wanyi Nie, Hsinhan Tsai, Jean-Christophe Blancon, Fangze Liu, Costas C. Stoumpos, Boubacar Traore, Mikael Kepenekian, Olivier Durand, Claudine Katan, Sergei Tretiak, Jared Crochet, Pulickel M. Ajayan, Mercouri G. Kanatzidis, Jacky Even, and Aditya D. Mohite**

Hybrid perovskites are on a trajectory toward realizing the most efficient single-junction, solution-processed photovoltaic devices. However, a critical issue is the limited understanding of the correlation between the degree of crystallinity and the emergent perovskite/hole (or electron) transport layer on device performance and photostability. Here, the controlled growth of hybrid perovskites on nickel oxide (NiO) is shown, resulting in the formation of thin films with enhanced crystallinity with characteristic peak width and splitting reminiscent of the tetragonal phase in single crystals. Photophysical and interface sensitive measurements reveal a reduced trap density at the perovskite/NiO interface in comparison with perovskites grown on poly(3,4-ethylene dioxy thiophene) polystyrene sulfonate. Photovoltaic cells exhibit a high open circuit voltage (1.12 V), indicating a near-ideal energy band alignment. Moreover, photostability of photovoltaic devices up to 10-Suns is observed, which is a direct result of the superior crystallinity of perovskite thin films on NiO. These results elucidate the critical role of the quality of the perovskite/hole transport layer interface in rendering high-performance and photostable optoelectronic devices.

Among all the solution-processed thin-film optoelectronic material technologies investigated over the past 2 decades, organic–inorganic (or hybrid) methylammonium lead tri-iodide ($MAPbI_3$) perovskites have emerged as clear front-runners with proof-of-concept high performance devices demonstrated for a broad range of applications.[1–8] The MAPbI3-based photovoltaic devices have demonstrated constantly increasing power conversion efficiency (PCE), which now exceeds 22%[9,10] and is steadily approaching that of single-junction monocrystalline Silicon (c-Si) solar cells. Although the record for the highest efficiency perovskite solar cell was achieved using a mesoporous titania (TiO2)-based architecture,[10–12] photovoltaic devices employing a simple planar architecture are closing in with the highest reported efficiency of 20%.[6,13,14] Great efforts have been put forth for

Dr. W. Nie, H. Tsai, Dr. J.-C. Blancon, Dr. F. Liu, Dr. A. D. Mohite
Materials Physics and Application
Los Alamos National Laboratory
Los Alamos, NM 87545, USA
E-mail: wanyi@lanl.gov; amohite@lanl.gov

H. Tsai, Prof. P. M. Ajayan
Materials Science and Nano-engineering
Rice University
Houston, TX 77005, USA

Dr. C. C. Stoumpos, Prof. M. G. Kanatzidis
Department of Chemistry
Department of Materials Science and Engineering
Northwestern University
Evanston, IL 60208, USA

Dr. B. Traore, Dr. M. Kepenekian, Dr. C. Katan
Institut des Sciences Chimiques de Rennes
ISCR UMR 6226
CNRS
Université de Rennes 1
Rennes 35042, France

Prof. O. Durand, Prof. J. Even
Fonctions Optiques pour les Technologies de l'Information
FOTON UMR 6082
CNRS
INSA de Rennes
Rennes 35708, France

Dr. S. Tretiak
Theoretical Chemistry and Molecular Physics Division
Los Alamos National Laboratory
Los Alamos, NM 87545, USA

Dr. J. Crochet
Physical Chemistry and Applied Spectroscopy Division
Los Alamos National Laboratory
Los Alamos, NM 87545, USA

DOI: 10.1002/adma.201703879

achieving highly efficient planar solar cells by exploring for potential ideal contact layers.[15] In addition, it is now realized that the next steps in advancing hybrid perovskite-based materials toward a viable photovoltaic technology will require simultaneously improving both the overall efficiency and also intrinsic stability. Therefore, optimal selection of electron and hole transport layers (HTLs) will require close consideration such that they not only boost the efficiency but also impart stability against constant full-spectrum solar irradiation and environmental effects. Moreover, there is also a stronger consensus that effects, such as hysteresis,[16–18] ion migration[19–23] and structural instability[24,25] with light soaking are strongly correlated to the degree of crystallinity of the hybrid perovskite thin films, grain boundaries, and interface passivation.[20,21,25–30]

There have been a few encouraging reports on using metal oxides as electron and hole transport layers, while improving the charge transport properties in devices, those oxides were found to act as protective barriers against the environment.[31–35] For instance, Han and co-workers showed that using modified compact TiO_2 as the electron transport layer (ETL) and nickel oxide (NiO_x) as the HTL resulted in much improved stability for devices when encapsulated with glass.[36] More recently, You et al. showed that using NiO_x as an HTL can lead to much improved stability against water and oxygen when the devices were stored in the dark.[35] Kim et al. reported similar results, where Cu doped NiO_x resulted in improved stability for devices stored in the dark.[37] These reports demonstrate the potential of metal oxide films as charge transport layers for high performance photovoltaics that improve protection from the environmental conditions. However, several fundamental questions remain unanswered. For example, there have been no studies investigating the role of crystallinity, structure, and the resulting interface quality of $MAPbI_3$ thin films grown on top of metal oxide layers, which are critical for both performance and stability. Moreover, in most cases, the environmental stability was evaluated by storing the devices in the dark without constant light soaking. There have been several studies which have now suggested that constant light soaking is critical for evaluating device stability during operation and cause severe photodegradation due to local phase segregation[25] or electronic trap states or vacancy formation.[28,37–40] In fact, in our recent work,[41] using the poly(3,4-ethylene dioxy thiophene) polystyrene sulfonate (PEDOT:PSS)-based planar photovoltaic devices, we showed that constant light soaking with calibrated 1-Sun light source triggers reversible photocurrent degradation within an hour and due to formation of light-activated trap states that are initialized at the interface between the perovskite/HTL or at defects within the bulk film.[42,43]

Here, we demonstrate that perovskite thin films grown on Li-doped NiO (LiNiO) by hot-casting method[44,45] exhibit enhanced crystallinity and structural ordering reminiscent of single crystalline perovskites. In-depth analyses on crystallography and film morphology studies reveal the formation of a highly crystalline and characteristic peak splitting indicative of a stabilized tetragonal phase of $MAPbI_3$ unique to single crystalline perovskites with comparable Bragg peak broadenings. We show that the overall quality of the perovskite film on LiNiO and the emergent interface is strongly correlated to the observation of reproducible, hysteresis free, high-efficiency devices with an average efficiency of ≈17% (active area 0.5 cm^2) mainly arising from a substantial enhancement in the average V_{OC} from ≈0.9 to ≈1.10 V. Extensive spectroscopy and device characterization reveals the suppression of the nonradiative decay through deep-level traps and improved transport of charge carriers through the bulk and the interfacial contacts. A direct implication of enhanced crystallinity and reduced interface trap density is the suppression of the photodegradation process usually observed with device using PEDOT:PSS as HTL[41] or less crystalline thin films on LiNiO (using room temperature casting method with postannealing), thus imparting the much-desired intrinsic photostability under continuous light soaking and up to 10-Suns without UV filter.

Figure 1 illustrates the thin-film morphology and crystallinity of $MAPbI_3$ thin film (310–370 nm in thickness) grown on top of LiNiO layer by hot-casting method (see Experimental Section for preparation details) using scanning electron microscopy (SEM) and grazing incidence X-ray diffraction (GIXRD). As a comparison, we also deposit $MAPbI_3$ on top of PEDOT:PSS (40 nm) under identical casting conditions with comparable perovskite film thicknesses of ≈310–370 nm determined using thin-film profilometry and cross-sectional SEM image as illustrated in Figure 1b. We emphasize that in contrast to other methods for the growth of perovskite thin films, the hot-cast $MAPbI_3$ on the substrates (both LiNiO and PEDOT:PSS) forms a bulk-like thin film with no apparent grain boundaries traversing through the film thickness and extends uniformly in the lateral direction, thus making it ideal for the fabrication of planar solar cells.

The crystallinity of the perovskite film was then characterized using GIXRD as illustrated in Figure 1c along with the spectrum for $MAPbI_3$ grown on PEDOT:PSS surface under the same processing condition. As a reference, the single crystal $MAPbI_3$ spectrum (taken from ref. [46]) is shown in Figure 1c (black curve) where the diffraction peaks can thus be identified. Deeper analysis of the GIXRD pattern and peak indexing reveals that GIXRD patterns can be identified and properly matched to peaks observed in single crystals of $MAPbI_3$. In addition, various splitting for the typical peaks from the tetragonal phase, i.e., (112) and (200) or (004) and (220) as shown in the Figure 1c (right panels), clearly indicates the presence of a stabilized tetragonal phase with enhanced crystallinity. In sharp contrast, the perovskite thin films fabricated on PEDOT:PSS only exhibit (100) and (200) peaks (cubic phase indexation) and do not exhibit these peak splitting between 20° and 27° consistent with previous observations using other thin-film processing methods[4,19,47] (see Figure S1 in the Supporting Information). To further examine the structure and crystalline quality, we performed a detailed 2D Grazing incidence wide angle X-ray scattering (GIWAXS) analysis on $MAPbI_3$ thin films grown on both PEDOT:PSS and LiNiO layers (see Figure S2a in the Supporting Information), which is important for understanding the observed peak splitting. The main perovskite peaks can be labeled accordingly on the GIWAXS map consistent with the GIXRD spectrums in both of the cases, with typical peaks of the tetragonal phase in the case of LiNiO substrates only. We further did a line-cut analysis in the main (110) peak (Figure S2b in the Supporting Information), the $MAPbI_3$ grown on LiNiO shows a peak splitting while the one on PEDOT:PSS only show

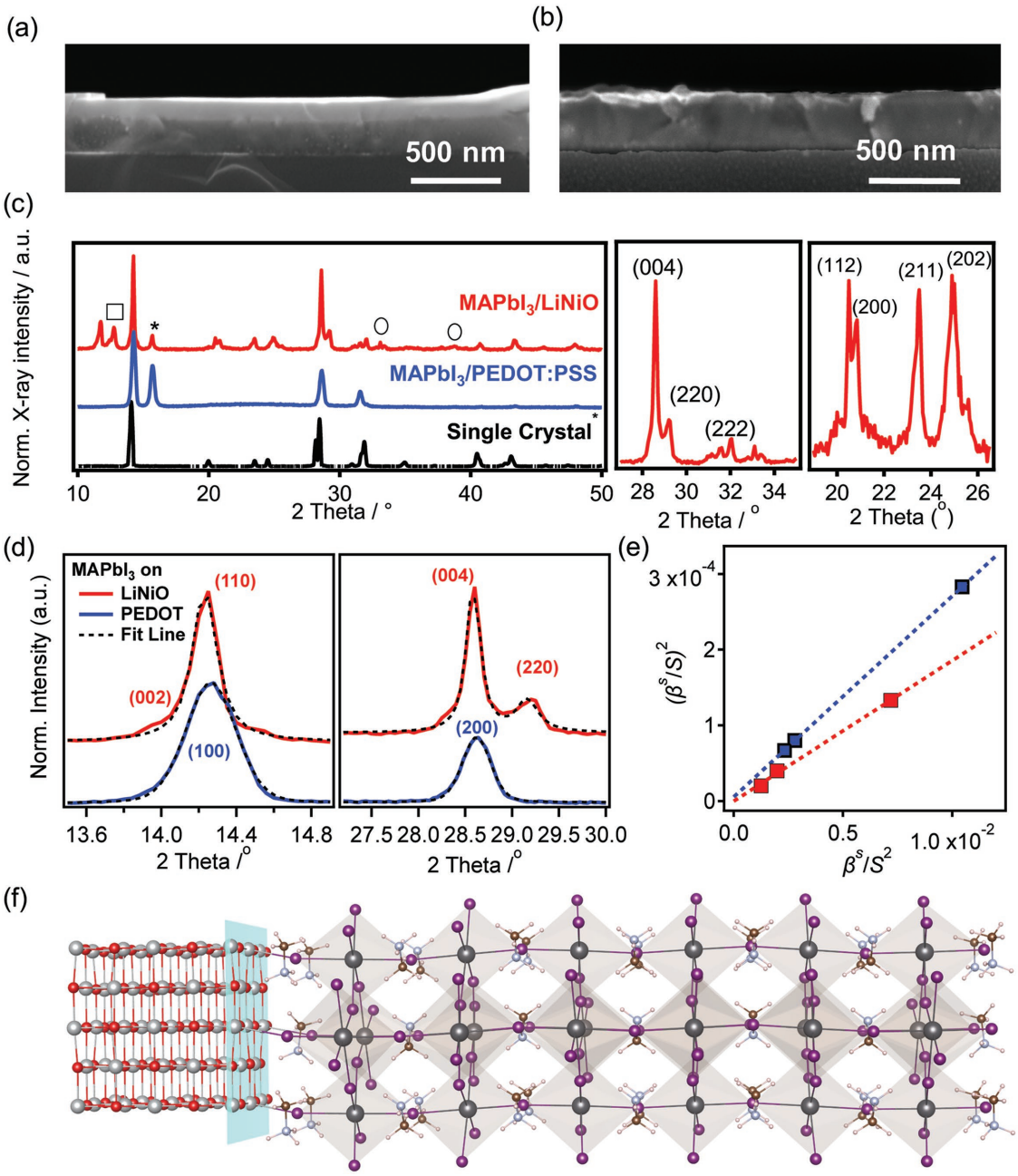

Figure 1. a,b) Cross-sectional view of hybrid perovskite thin film by hot-casting method on LiNiO and PEDOT:PSS coated substrates respectively; c) GIXRD pattern for $MAPbI_3$ hot-cast thin-film on LiNiO as compared with on PEDOT:PSS substrates and single crystal diffraction pattern [taken from ref. [38] with indexing]. Right panels are zoomed in patterns in a specific 2θ range. The peaks labeled with * refer to $MAPbCl_3$ phase and □ are PbI_2 phase, o are peaks from LiNiO substrates (see also GIWAXS line cuts in Figure S10, Supporting Information); d) zoom-in profiles for (100) and (200) peaks (on PDOT-PSS: labeled using the cubic phase indexation, while on LiNiO, the peaks are labeled using the tetragonal phase indexation) for line profile (integral breadths-IB) analysis with pseudo-Voigt fits taking into account $\lambda_{K\alpha_1}$ and $\lambda_{K\alpha_2}$ wavelengths; e) IB analysis using Halder–Wagner plots, where β is the integral breadth of the diffraction peak and S is defined as $S = \frac{2\sin\theta}{\lambda}$. f) Structure of the $MAPbI_3$/NiO (100) model interface based on density functional theory (DFT) calculations. The structure shows Ni—I bonds at the interface region. For the colors, red for O, gray for Ni, purple for I, light blue for N, brown for C, and pink for H.

a merged broad peak. We note that typically in amorphous thin film the observed splitting of the peaks like in our case is absent because features are often masked due to inhomogeneous peak broadening and as a result most of the weak Bragg reflections disappear. We also conducted a detailed analysis on the diffraction peak full width at the half maximum (FWHM) from the GIXRD pattern in Figure 1c and are summarized in Figure 1d,e. For the case of $MAPbI_3$ on PEDOT:PSS surface, the XRD peaks are broader for both of the (100) and (200) peaks (cubic phase indexation), thus making it challenging to resolve

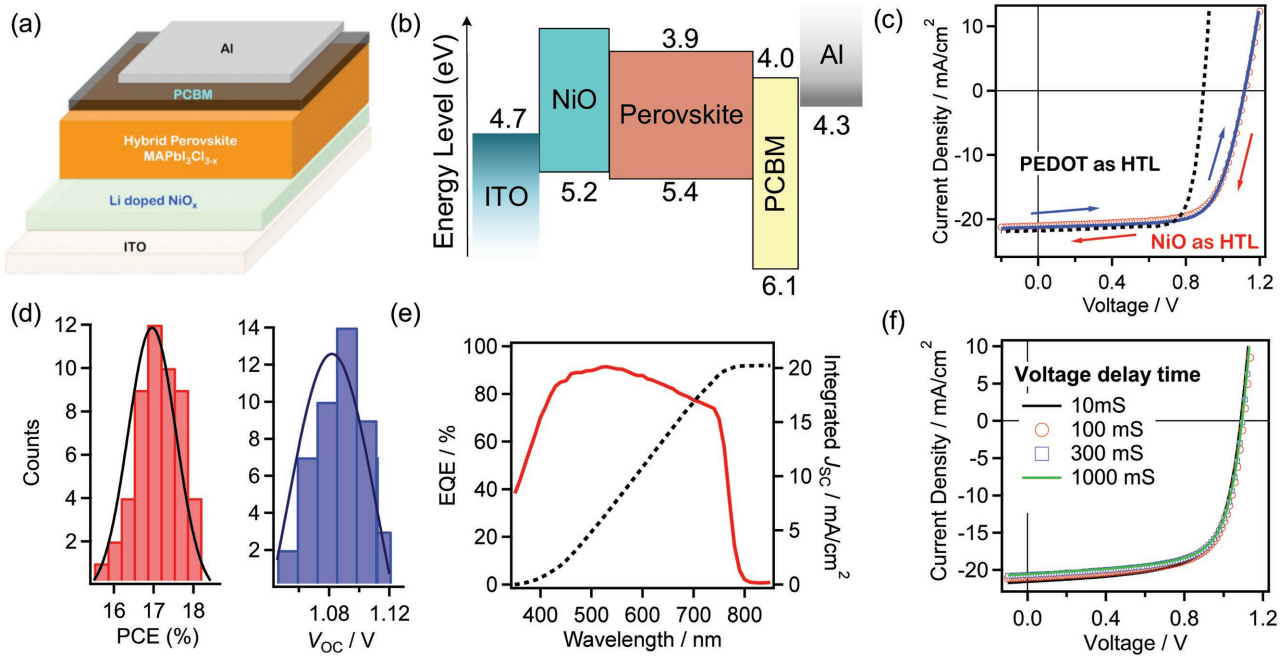

Figure 2. a) Scheme for planar device structure; b) energy diagram for each layers in the device; c) the current–density voltage scan for champion LiNiO device under 1-Sun illumination as compared to the PEDOT-based device (black dotted line). The hysteresis for LiNiO device is also tested by performing the forward scan (red) and reverse scan (blue) and the two curves overlay on top of each other. d) Histogram statistical curves for LiNiO device PCE (left) and V_{OC} (right) over 50 device from different batches, e) EQE of the planner solar cell using LiNiO (solid line) and PEDOT (dashed line) as HTL, respectively. f) The light *J*–*V* curves under 1 Sun for a typical $MAPbI_3$/LiNiO device at different voltage delay time (scan rate).

the weaker reflections. The results of the integral breadths (IB) analysis with pseudo-Voigt fits[48,49] are illustrated in Figure 1e (the Methods section is described in Equations S1–S5 and Figure S1 in the Supporting Information). From the peak analysis in Figure 1e, the correlation lengths are found equal to 48.5 nm for $MAPbI_3$ hot-cast thin film on LiNiO and 33.9 nm on PEDOT:PSS substrate. Error bars are estimated around 1 nm. More, an additional broadening is related to microstrain distribution in the case of PEDOT:PSS, whereas this distribution is negligible for LiNiO. It clearly implies that the thin-film $MAPbI_3$ on LiNiO exhibits enhanced crystallinity by comparison to the sample grown on PEDOT:PSS. This observation is also consistent with the presence of peak splitting characteristic of the tetragonal phase.

Such enhancement in the crystalline quality of $MAPbI_3$ on LiNiO surface is likely due to the different surface nature of LiNiO surface as revealed by the atomic force microscopy images (Figure S5, Supporting Information) and contact angle measurement (Figure S6 in the Supporting Information). The results suggest that LiNiO has crystalline surface with multidomain that can assist the perovskite nucleation process during film formation.[50,51] In contrast, the PEDOT:PSS surface exhibits amorphous feature which can impede crystal growth. Furthermore, the surface energy of LiNiO is higher than PEDOT:PSS surface as revealed by the contact angle measurement. The LiNiO has higher contact angle when processing with the carrier solvent, leading to a "nonwetting" surface that can assist the crystal formation, which is consistent with literature report.[52] However, we notice that employing room temperature casting method to grow $MAPbI_3$ on the LiNiO surface does not lead to highly crystalline thin film. This suggests that both nucleation sites from the surface and processing energy are important during the crystalline film formation. Moreover, the good match between tetragonal $MAPbI_3$ and LiNiO is further supported using first-principles computational modeling (see Figure 1f, Figure S7 and additional discussion in the Supporting Information).

Motivated by the superior crystallinity for the thin films of $MAPbI_3$ grown on LiNiO, we fabricated photovoltaic devices to evaluate their optoelectronic properties. **Figure 2** summarizes the solar cell device structure and performance for the perovskite thin films on LiNiO as HTL. Figure 2a illustrates the scheme for the planar device structure used in this study (from now on referred to as LiNiO device) along with the energy level alignments of the different layers (Figure 2b) with respect to the perovskite film derived from previous measurements.[53,54] Here, the LiNiO was spin coated and then sintered (see Methods section in the Supporting Information for processing details), followed by hot casting a layer of $MAPbI_3$ of 310 ± 20 nm using our recently published method.[41,44,55,56] 6,6-phenyl-C61-butyric acid methyl ester (PCBM) solution was spin coated on top of the hot cast $MAPbI_3$ thin film to serve as the ETL layer and the device was completed by thermally evaporating aluminum as the cathode. Here, the pristine NiO was doped using Li+ as a dopant for improving in conductivity by substituting Ni^{2+} by Li^{+}. We examined the crystalline structure with Li^{+} in the NiO thin film by GIXRD (in Figure S8 in the Supporting Information) and found the Li^{+} was incorporated into NiO lattice, possibly replacing the Ni^{2+} vacancy and thus increased the conductivity of the NiO film[57–59] measured by four-probe methods

(see Figure S8 in the Supporting Information). Figure 2c illustrates the photovoltaic performance obtained by measuring the current density–voltage curve (J–V) using an AM 1.5G solar simulator, calibrated using an NIST Silicon photodiode. For our champion LiNiO device, we obtained a V_{OC} ~ 1.12 V with a fill factor of 73.6 % and a short circuit current density (J_{SC}) of 21.79 mA cm^{-2}, which resulted in a peak PCE of ≈18%. To elucidate the role of lithium in the cell operation, we evaluated the film morphology of NiO without/with lithium doping and the perovskite film formation on those surfaces (results can be found in Figures S9–S10 in the Supporting Information). We found the perovskite thin film form similarly on both of the surface due to similar morphology of (Li)NiO surface. However, we found the power conversion efficiency is improved by about 40% from 11% ± 0.85% in NiO device to 17.43% ± 0.44% with lithium incorporated NiO device, and peaks at around 5% doping by atomic ratio. And such increase is found to be related with the enhanced conductivity of the NiO thin film, as discussed in Figures S11 and S12 in the Supporting Information.

Figure 2d shows the degree of reproducibility captured in a histogram of PCE yielding an average value of 17.0% and V_{OC} of 1.1 V respectively for over 50 LiNiO devices with an active area of 0.5 cm^2. Figure 2e illustrates the external quantum efficiency (EQE) of a typical LiNiO device, which translates to a near equivalent short circuit current density (20.23 mA cm^{-2}) with mismatch of ≈7%. The LiNiO devices exhibit negligible hysteresis in their J–V characteristics as shown in Figure 2f.

Next, we investigate photophysical properties in perovskite thin films grown on LiNiO and directly compare them with that on PEDOT:PSS. We characterize the optical properties of $MAPbI_3$ film grown on LiNiO by photoluminescence (PL) and time-resolved PL (TRPL) using an excitation energy (wavelength) of 1.80 eV (690 nm). We ensure that the PL signal and TRPL response before and after laser exposure as described in ref. [40] does not change appreciably to affect measurement and the derived conclusions (see detailed Methods section in the Supporting Information). The typical absorbance response for $MAPbI_3$/LiNiO sample is plotted in **Figure 3**a, which is concomitant with the EQE measured in Figure 2e. The PL for $MAPbI_3$ thin films both on LiNiO and PEDOT is shown in Figure 3a (measured without the electron transporting layer and Al back contact). The optical bandgaps obtained from both the absorption and photoluminescence yield 1.614 ± 0.002 eV (768 ± 1 nm) for $MAPbI_3$/LiNiO, as compared

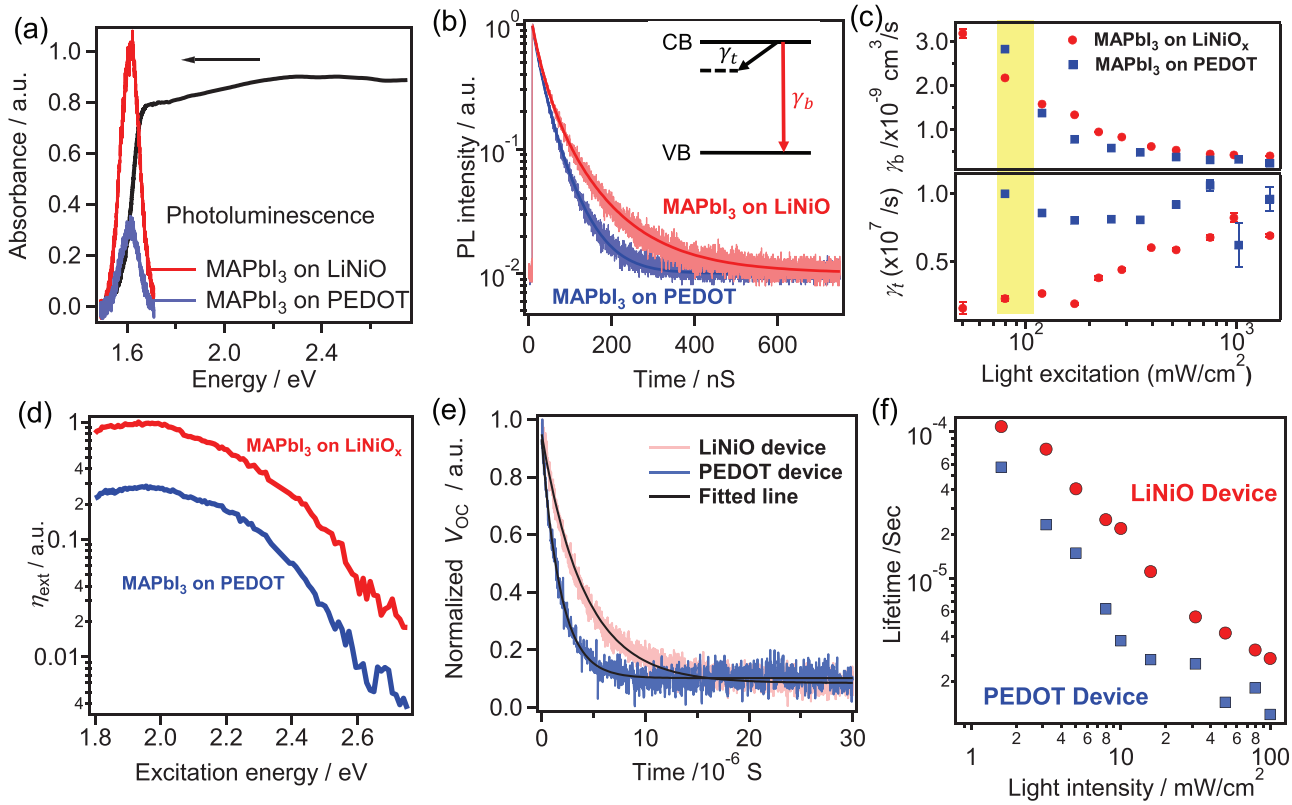

Figure 3. a) Optical absorbance for perovskite thin film devices (black). Photoluminescence of perovskite thin films on both LiNiO (red) and PEDOT:PSS (blue). Color code is kept for the other panels. b) Time-correlated single photon counting histograms of the PL (light colors) exciting at 1.80 eV (690 nm) under about 1-Sun light intensity and the recombination models (dark colors) for both samples. (inset) Schematic representation of the modeling of the dynamics of light emission (see text for details). γ_b is the bimolecular coefficient and γ_t the trap-assisted nonradiation relaxation rate. c) Bimolecular coefficient (top) and trap-assisted relaxation rate (bottom) as a function of photoexcitation intensity, derived from the fit of the data. The highlighted area represents the 1-Sun equivalent condition. Error bars do not include the maximum 10% error from the absorption. d) External photoluminescence efficiency as a function of excitation energy and detecting at 1.62 eV. e) TPV decay curve under white bias light with intensity equivalent to 1-Sun (100 mW cm^{-2}) generated by LED with small red light perturbation. f) Charge recombination lifetime determined by TPV as a function of light intensity for LiNiO (red) and PEDOT (blue) as HTL.

to 1.612 ± 0.002 eV (769 ± 1 nm) for PEDOT:PSS as HTL and the Stokes shift is negligible (<2 meV) in both cases indicating good homogeneity of the perovskite films. Similar value of the optical bandgap for both samples is indicative of the same stoichiometric composition of perovskite as compared to the films on a glass substrate.[44]

To quantify the charge recombination processes in both samples, we performed TRPL on $MAPbI_3$ grown on both of the substrates, which monitors the decay of the nonequilibrium carrier density $N(t)$ after photoexcitation and relaxation at bandedge as described in Figure 3b, inset. The TRPL data can then be well fitted using Equations (1) and (2)

$$\dot{N} = -\gamma_b N^2 - \gamma_t N \tag{1}$$

$$I_{PL} \sim N^2 \text{ (from Figure 3b)} \tag{2}$$

where γ_b is the bimolecular coefficient, which probes the rate of electron–hole recombination through the bandgap, and γ_t is the nonradiative decay rate through deep trap.[45] Based on this model, we therefore extracted the γ_b and γ_t values as a function of excitation intensity as shown in Figure 3c. From the results, it is clear that both perovskites films grown on LiNiO and PEDOT operate in a regime dominated by bimolecular recombination– the bimolecular coefficients γ_b are comparable (Figure 3c, top panel), of the order of 1.5×10^{-9} cm^3 s^{-1} at solar-equivalent photoexcitation intensity (around 100 mW cm^{-2} as highlighted in the figure). However, an important finding is that we observe a significant reduction of the nonradiative decay rate γ_t in the case of $MAPbI_3$/LiNiO (Figure 3c, bottom panel) in comparison to $MAPbI_3$/PEDOT:PSS samples at low powers. This difference reaches almost one order of magnitude at light intensity equivalent to 1-Sun. The TRPL results indicate that in the operation regime of solar cells, shallow electronic impurity states are passivated, photoexcited carriers undergo a bimolecular recombination process as the main recombination pathway.[45] However, in the case of LiNiO device, photoexcited free carriers have a much lower probability to be quenched by the deeper electronic impurities (Figure 3b,c) in comparison to the PEDOT:PSS device, especially close to the solar cell operation (≈100 mW cm^{-2}, highlighted in Figure 3c). We attribute such reduced trap assisted recombination to be due to both superior thin-film crystallinity of $MAPbI_3$ grown on LiNiO and the superior quality of the resulting interface possibly due to the passivation effect from the LiNiO interface. Deep level traps are well known to contribute to the overall trap density (bulk and interface) significantly as measured using capacitance and impedance spectroscopy. However, for the $MAPbI_3$ is grown on LiNiO, these trap states are passivated and thus suppress the nonradiative recombination pathways as revealed using time-resolved photoluminescence experiments described in Figure 3 and in good agreement with the impedance measurement (Figures S13 and S14 in the Supporting Information).

To further understand the origin of the increase in the V_{OC}, we also examine the photoemission properties of the perovskite thin films, in particular, the internal quantum efficiency (η_{int}), and the external quantum efficiency (η_{ext}). Figure 3d shows the relative η_{ext}, i.e., the ratio between the photoluminescence intensity and the absorption, as a function of excitation laser energy (see also Methods section in the Supporting Information). η_{ext} yields a nearly fourfold increase for $MAPbI_3$ on LiNiO as compared to the $MAPbI_3$ grown on PEDOT. Owing to the reciprocity relationship between open-circuit voltage and external PL efficiency[47] described by Equation (3)

$$V_{OC} = V_{OC,\,ideal} - kT\left|\ln\left(\eta_{ext}\right)\right| \tag{3}$$

an increase of η_{ext} does contribute to the increase of V_{OC} coming from both lowered trap density and fast charge transfer rate. However, a three- to fourfold increase in η_{ext} corresponds to a relatively modest contribution to the rise in V_{OC} (≈40 meV) as compared to about 200 meV in solar cells. This suggest that the main contribution to the V_{OC} increase in devices with LiNiO as HTL as compared to their PEDOT counterparts, results from a superior quality of the interface with decrease of interface deep-trap states, and better band alignment of the LiNiO Fermi level with the valence band of the perovskites (Figure 2b) (see Figure S15, Supporting Information for detailed discussions).

In summary, our observations in PL and device characterizations support the hypothesis of a smaller density of deep electronic impurities in the bulk and at the perovskite/LiNiO interface. We emphasize from our observations that both the work function alignment with $MAPbI_3$ and the quality of the $MAPbI_3$ thin film (reduced trap-assisted recombination) play a dominant role, which manifests as a large increase in the open circuit voltage.

Next to explicitly evaluate the quality of the perovskite/HTL interface, we performed transient photovoltage decay (TPV) measurements (Figure 3e,f), which gives the rate of recombination of the photoexcited charge at the semiconductor/contact interface during device operation condition. This method has been previously applied to directly prove the quality of the interface in hybrid perovskites and other material systems.[59,60] At open circuit condition, no charges are collected in the outer circuit; the photoexcited excess carriers (minority carrier) generated by the small perturbation under equilibrium charge density produced by white light first reaches the electrode and then recombine near one of the contact interfaces when the light pulse is off, which is observed as a decay in photovoltage.[61] The lifetime fitted from the decay curve is proportional to the rate of charge recombination near the interface under open circuit condition. Figure 3e shows a typical TPV decay curve under white light bias for both LiNiO and PEDOT:PSS as HTL. All the curves can be fitted well with a single exponential decay indicating that bimolecular recombination is the dominant process during device operation in both of the devices. This is in agreement with the pure bimolecular process reported above by optical spectroscopy in thin films. We further measured the decay curve as a function of background white light bias intensity. The fitted effective-lifetime values are shown in Figure 3f. As anticipated, the lifetime values for both of the devices decreases with raising light intensity due to increase in the density of photogenerated carriers.[62] By comparing the two devices, for all the light intensities, the LiNiO device has longer recombination lifetime under open circuit condition ranging from 3 μs at 100 mW cm^{-2} to 100 μs at 10 mW cm^{-2}. In contrast, the PEDOT:PSS-based device has a much shorter lifetime in the range of 1–50 μs in the same measurement

range. Because the device is fully depleted as revealed using capacitance-voltage measurement, (see Figure S14c in the Supporting Information), the majority charge is localized near the $MAPbI_3$/contact interface, where carrier recombination is spatially most dominant. Therefore, the TPV describes the charge recombination through the internal resistor across the two electrodes of the device, the recombination lifetime is thus dominated by the surface recombination.[61] The longer lifetimes in LiNiO device therefore indicate a lower recombination rate compared to the PEDOT:PSS device, which arises from the reduced trap-assisted recombination near that interface. The result is consistent with capacitance measurements, which also imply a relatively reduced interface trap density in the case of perovskite/LiNiO. The reduced trap-assisted recombination and longer electron lifetime therefore allow the photoexcited charges to be extracted more efficiently before they recombine during device operation, which manifests as a higher open circuit voltage.

Finally, in order to evaluate the role of enhanced bulk and interface crystallinity on photostability, we performed measurements with continuous light soaking with a full spectrum with air mass 1.5 Global (AM 1.5G) filter of the perovskite solar cells with LiNiO and compared them to those fabricated using PEDOT:PSS. We recorded the device performance as a function of illumination time and light power as illustrated in **Figure 4**. We first look at the V_{OC} and observe that both the devices do not degrade over time with light soaking (see Figure S16 in the Supporting Information). However, for the PEDOT:PSS-based devices, there is a significant increase from 0.79 to 0.95 V in the V_{OC} over the first 30 min of light soaking, which has been previously attributed to an initial trap filling.[63] In contrast, such trap-filling process is not observed in the LiNiO device and it reaches ≈1.1 V almost instantaneously with illumination and thereafter remains flat over the testing period (2 h), which clearly indicates that the defects at the perovskite/LiNiO are appreciably lower. Next, we monitor the changes in the J_{SC} under constant illumination, as illustrated in Figure 4a. The LiNiO device exhibits excellent stability over 10 h constant 1-Sun illumination without additional UV filters. To further evaluate the photocurrent stability, we performed accelerated test by monitoring the J_{SC} under various light intensities (1-Sun to 10-Suns illumination), as shown in Figure 4b. The $MAPbI_3$/LiNiO device shows a stable current output for up to 10-Suns illumination during the testing period. The degradation only sets in after an hour of light soaking at an order of magnitude higher intensities of 10-Suns, most likely due to an increase in temperature[41,45] of the solar cell.

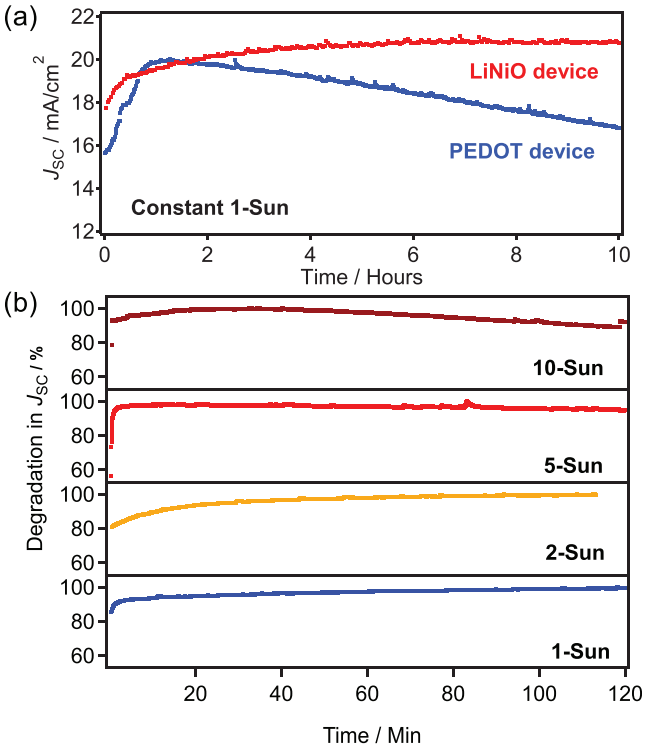

Figure 4. Device stability test under constant illumination with a full spectrum AM1.5G source and under various light intensity. a) Time evolution of the J_{SC} under short circuit condition with AM 1.5G under 1-Sun illumination on PEDOT:PSS and LiNiO devices. c) J_{SC} time evolution of $MAPbI_3$/LiNiO device growing by hot-casting method under different light intensities.

We recall that the photodegradation in the J_{SC} was attributed to the formation of light-activated metastable trap states (small polarons[64]) and their accumulation in the perovskite layer over several minutes to hours, resulting in a slow decrease of photocurrent over time under 1-Sun illumination condition.[40] These light-activated trap states appear as deep-level traps formed by a nonradiative relaxation of photoexcited carriers, leading to the degradation of photocurrent in devices with PEDOT (Figure 4a,b). They act like "seeds" that with continuous light soaking over time lead to the accumulation of trap states and formation of charged regions, and such degradation process is strongly illumination power dependent. In the case of growing highly crystalline $MAPbI_3$ on LiNiO, such threshold has been pushed much further down in time when illuminating under 1-Sun. And for higher power illumination, the LiNiO device also exhibits much more robust performance up to 10-Suns light power. These experiments indeed proved that the highly crystalline $MAPbI_3$ and improved interface greatly hinder those metastable trap states formation and thus leading to photostable output. Through this work, we show that improving the crystalline quality of the $MAPbI_3$ material and emergent interface leads to a strong suppression of the deep level defects and leads to much improved charge carrier transport in the bulk and through the interfaces. Altogether, this constitutes an important step toward achieving photostable perovskite thin films not just for photovoltaics but for any conceivable optoelectronic devices.

In this study, we report efficient, hysteresis-free, and photostable hybrid perovskite solar cells enabled by growing highly crystalline $MAPbI_3$ layer using hot-casting method on lithium-doped NiO surface. We evaluated the $MAPbI_3$ crystalline structure by GIXRD and microscopy and found a stable tetragonal phase perovskite can be formed on LiNiO. Direct correlations between the degree of crystallinity of perovskite film and improved electronic properties of devices are elucidated via systematic investigations using crystallography, DFT, spectroscopy, and device characterizations. In particular, increased V_{OC} in LiNiO devices are found to be directly related with better interface energy level alignment, suppressed trap-assisted

recombination in the bulk and at the interfacial contacts. Moreover, such devices represent excellent photostability under continuous light soaking when exposed to simulated sunlight (AM 1.5G source with no UV filters) and can withstand up to 5-Suns of light intensity. This is a consequence of high degree of thin film crystallinity and clean interface with reduced trap density on LiNiO surface. As conclusion, we found the structure–property relationships play a crucial role for achieving photostable, reliable high efficiency perovskite-based thin-film optoelectronic devices. We anticipate that this work will lead to further efforts on improving the thin-film crystallinity as well as interface qualities, and as a result, the overall physical properties. This shall progressively push the field of hybrid perovskites toward the realization of technologically viable stability.

Experimental Section

LiNiO Solution Preparation: LiNiO solution was prepared according to literature, by dissolving 0.1 M nickel (II) acetate tetrahydrate (99.998%, Sigma-Aldrich) in absolute ethanol (Sigma-Aldrich) with monoethanolamine (MEA). The molar ratio of Ni^{2+} and MEA was kept to be 1:1. After the solution was stirred at 60 °C for 1 h, a clear and deep green solution was formed. The lithium nitrate was added at *X* molar% (*X* = 0, 2, 5, 10, and 20) was added as Li^{+} source to improve the conductivity of the NiO film.

Perovskite Solution: The $MAPbI_3$ precursor was prepared by dissolving lead iodide (PbI_2) and methylammonium iodide (99.8% Sigma-Aldrich) and methylammonium chloride (molar ratio = 1:0.5:0.5) in anhydrous N, N-dimethylformamide with molar concentration of 0.43 M. The prepared solution was stirred for at least 24 h at 70 °C before using.

Device Fabrication: The patterned fluorine-doped tin oxide (FTO, Thin Film Device Inc) slides were first cleaned in ultrasonication bath in water, acetone, and isopropyl alcohol for 15 min, respectively. The substrates were then dried under nitrogen air flow followed by 30 min baking on hot plate in air for 30 min. The dried substrates were treated by oxygen plasma for 3 min before coating. The stock solution of LiNiO precursor or PEDOT:PSS (Clevis 4083) was coated by spin coating at 3000 and 5000 rpm respectively for 40 s to serve as hole transporting layer (HTL). The substrates were dried at 150 °C for 20 min in the air. The LiNiO/FTO substrates were then taken into a tube furnace for 450 °C sintering in ambient condition. The coated substrates were then transferred into an argon-filled glovebox for perovskite and top contact deposition. The $MAPbI_3$ layers were produced by hot-casting method, where the LiNiO or PEDOT:PSS coated substrates were first heated at 150 °C and then quickly transferred to the spin coater chunk and spinning process was started immediately after dropping the precursor on the substrates at 5000 rpm without ramping for 20 s. The film color changed from transparent to dark brown almost instantaneously after solvent escaped. The obtained $MAPbI_3$ on HTL/FTO substrates were then loaded into a vacuum chamber for aluminum deposition after coating by PCBM solution as electron transporting layer.

Solar Cell Characterization: The solar cells were characterized by taking current–voltage curves under solar simulator with light intensity equivalent to 1-Sun (100 mW cm^{-2}) with air mass 1.5 G filter. The devices were masked to reduce error induced edge effect. The external quantum efficiencies were collected by illuminating the device under monochromatic light using a tungsten source (chopped at 150 Hz) while collecting the photocurrent by lock-in amplifier in AC mode. The light source spectrum response was corrected by calibrated silicon diode (FDS1010, Thorlab).

Supporting Information

Supporting Information is available from the Wiley Online Library or from the author.

Acknowledgements

The work at Los Alamos National Laboratory (LANL) was supported by DoE Office of Basic Energy Sciences Work Proposal 08SPCE973 (W.N., J-C.B. and A.D.M.) and by the LANL LDRD program (A.D.M. and S.T.). This work was done in part at the Center for Integrated Nanotechnologies, an Office of Science User Facility. The GIWAXS maps were done with help of Dr. Joseph W. Strzalka and use of sector 8-IDE in Advanced Photon Source at Argonne National Laboratory was supported by the US Department of Energy, Office of Science, Office of Basic Energy Sciences. The simulation work was performed using HPC resources from GENCI-[TGCC/CINES/IDRIS] (Grant 2017-A0010907682). The work at ISCR is supported by Agence Nationale pour la Recherche (TRANSHYPERO project). B.T. acknowledges funding from the European Union's Horizon 2020 program, through an FET Open research and innovation action under grant agreement No 687008. C.C.S. and M.G.K. acknowledge the support under ONR Grant N00014-17-1-2231. The authors thank Prof. Osman M. Bakr (KAUST) for providing single crystal diffraction data.

Conflict of Interest

The authors declare no conflict of interest.

Keywords

crystallinity, LiNiO, perovskite solar cells, photostability

Received: July 12, 2017
Revised: October 7, 2017
Published online: December 11, 2017

[1] M. M. Lee, J. Teuscher, T. Miyasaka, T. N. Murakami, H. J. Snaith, *Science* **2012**, *338*, 643.
[2] J. Burschka, N. Pellet, S.-J. Moon, R. Humphry-Baker, P. Gao, M. K. Nazeeruddin, M. Gratzel, *Nature* **2013**, *499*, 316.
[3] C. C. Stoumpos, C. D. Malliakas, J. A. Peters, Z. Liu, M. Sebastian, J. Im, T. C. Chasapis, A. C. Wibowo, D. Y. Chung, A. J. Freeman, B. W. Wessels, M. G. Kanatzidis, *Cryst. Growth Des.* **2013**, *13*, 2722.
[4] N. J. Jeon, J. H. Noh, Y. C. Kim, W. S. Yang, S. Ryu, S. I. Seok, *Nat. Mater.* **2014**, *13*, 897.
[5] Z.-K. Tan, R. S. Moghaddam, M. L. Lai, P. Docampo, R. Higler, F. Deschler, M. Price, A. Sadhanala, L. M. Pazos, D. Credgington, F. Hanusch, T. Bein, H. J. Snaith, R. H. Friend, *Nat. Nanotechnol.* **2014**, *9*, 687.
[6] H. Zhou, Q. Chen, G. Li, S. Luo, T.-B. Song, H.-S. Duan, Z. Hong, J. You, Y. Liu, Y. Yang, *Science* **2014**, *345*, 542.
[7] Y. Fang, Q. Dong, Y. Shao, Y. Yuan, J. Huang, *Nat. Photonics* **2015**, *9*, 679.
[8] H. Zhu, Y. Fu, F. Meng, X. Wu, Z. Gong, Q. Ding, M. V. Gustafsson, M. T. Trinh, S. Jin, X. Y. Zhu, *Nat. Mater.* **2015**, *14*, 636.
[9] M. A. Green, K. Emery, Y. Hishikawa, W. Warta, E. D. Dunlop, *Prog. Photovoltaics: Res. Appl.* **2016**, *24*, 905.
[10] M. Saliba, T. Matsui, J.-Y. Seo, K. Domanski, J.-P. Correa-Baena, M. K. Nazeeruddin, S. M. Zakeeruddin, W. Tress, A. Abate, A. Hagfeldt, M. Gratzel, *Energy Environ. Sci.* **2016**, *9*, 1989.
[11] W. S. Yang, J. H. Noh, N. J. Jeon, Y. C. Kim, S. Ryu, J. Seo, S. I. Seok, *Science* **2015**, *348*, 1234.
[12] D.-Y. Son, J.-W. Lee, Y. J. Choi, I.-H. Jang, S. Lee, P. J. Yoo, H. Shin, N. Ahn, M. Choi, D. Kim, N.-G. Park, *Nat. Energy* **2016**, *1*, 16081.
[13] C. Bi, Q. Wang, Y. Shao, Y. Yuan, Z. Xiao, J. Huang, *Nat. Commun.* **2015**, *6*, 7447.

[14] M. Yang, T. Zhang, P. Schulz, Z. Li, G. Li, D. H. Kim, N. Guo, J. J. Berry, K. Zhu, Y. Zhao, *Nat. Commun.* **2016**, *7*, 12305.
[15] W. Nie, G. Gupta, B. K. Crone, F. Liu, D. L. Smith, P. P. Ruden, C.-Y. Kuo, H. Tsai, H.-L. Wang, H. Li, S. Tretiak, A. D. Mohite, *Adv. Sci.* **2015**, *2*, 1500024.
[16] H.-S. Kim, N.-G. Park, *J. Phys. Chem. Lett.* **2014**, *5*, 2927.
[17] Y. Shao, Z. Xiao, C. Bi, Y. Yuan, J. Huang, *Nat. Commun.* **2014**, *5*, 5784.
[18] W. Tress, N. Marinova, T. Moehl, S. M. Zakeeruddin, M. K. Nazeeruddin, M. Gratzel, *Energy Environ. Sci.* **2015**, *8*, 995.
[19] J. M. Azpiroz, E. Mosconi, J. Bisquert, F. De Angelis, *Energy Environ. Sci.* **2015**, *8*, 2118.
[20] C. Eames, J. M. Frost, P. R. F. Barnes, B. C. O'Regan, A. Walsh, M. S. Islam, *Nat. Commun.* **2015**, *6*, 7497.
[21] J. Xu, A. Buin, A. H. Ip, W. Li, O. Voznyy, R. Comin, M. Yuan, S. Jeon, Z. Ning, J. J. McDowell, P. Kanjanaboos, J.-P. Sun, X. Lan, L. N. Quan, D. H. Kim, I. G. Hill, P. Maksymovych, E. H. Sargent, *Nat. Commun.* **2015**, *6*, 8081.
[22] Y. Zhang, M. Liu, G. E. Eperon, T. C. Leijtens, D. McMeekin, M. Saliba, W. Zhang, M. de Bastiani, A. Petrozza, L. M. Herz, M. B. Johnston, H. Lin, H. J. Snaith, *Mater. Horiz.* **2015**, *2*, 315.
[23] Y. Yuan, J. Huang, *Acc. Chem. Res.* **2016**, *49*, 286.
[24] E. J. Juarez-Perez, R. S. Sanchez, L. Badia, G. Garcia-Belmonte, Y. S. Kang, I. Mora-Sero, J. Bisquert, *J. Phys. Chem. Lett.* **2014**, *5*, 2390.
[25] E. T. Hoke, D. J. Slotcavage, E. R. Dohner, A. R. Bowring, H. I. Karunadasa, M. D. McGehee, *Chem. Sci.* **2015**, *6*, 613.
[26] H. Yu, H. Lu, F. Xie, S. Zhou, N. Zhao, *Adv. Funct. Mater.* **2016**, *26*, 1411.
[27] F. Wang, W. Geng, Y. Zhou, H.-H. Fang, C.-J. Tong, M. A. Loi, L.-M. Liu, N. Zhao, *Adv. Mater.* **2016**, *28*, 9986.
[28] E. Mosconi, D. Meggiolaro, H. J. Snaith, S. D. Stranks, F. De Angelis, *Energy Environ. Sci.* **2016**, *9*, 3180.
[29] G. Grancini, A. R. Srimath Kandada, J. M. Frost, A. J. Barker, M. De Bastiani, M. Gandini, S. Marras, G. Lanzani, A. Walsh, A. Petrozza, *Nat. Photonics* **2015**, *9*, 695.
[30] Q. Chen, H. Zhou, T.-B. Song, S. Luo, Z. Hong, H.-S. Duan, L. Dou, Y. Liu, Y. Yang, *Nano Lett.* **2014**, *14*, 4158.
[31] M. Kaltenbrunner, G. Adam, E. D. Glowacki, M. Drack, R. Schwodiauer, L. Leonat, D. H. Apaydin, H. Groiss, M. C. Scharber, M. S. White, N. S. Sariciftci, S. Bauer, *Nat. Mater.* **2015**, *14*, 1032.
[32] C. Liu, K. Wang, P. Du, T. Meng, X. Yu, S. Z. D. Cheng, X. Gong, *ACS Appl. Mater. Interfaces* **2015**, *7*, 1153.
[33] W. Qiu, M. Buffière, G. Brammertz, U. W. Paetzold, L. Froyen, P. Heremans, D. Cheyns, *Org. Electron.* **2015**, *26*, 30.
[34] J. Choi, S. Song, M. T. Hörantner, H. J. Snaith, T. Park, *ACS Nano* **2016**, *10*, 6029.
[35] J. You, L. Meng, T.-B. Song, T.-F. Guo, Y. Yang, W.-H. Chang, Z. Hong, H. Chen, H. Zhou, Q. Chen, Y. Liu, N. De Marco, Y. Yang, *Nat. Nanotechnol.* **2016**, *11*, 75.
[36] W. Chen, Y. Wu, Y. Yue, J. Liu, W. Zhang, X. Yang, H. Chen, E. ZBi, I. Ashraful, M. Gratzel, L. Han, *Science* **2015**, *350*, 944.
[37] J. H. Kim, P.-W. Liang, S. T. Williams, N. Cho, C.-C. Chueh, M. S. Glaz, D. S. Ginger, A. K. Y. Jen, *Adv. Mater.* **2015**, *27*, 695.
[38] Y. Tian, A. Merdasa, M. Peter, M. Abdellah, K. Zheng, C. S. Ponseca, T. Pullerits, A. Yartsev, V. Sundström, I. G. Scheblykin, *Nano Lett.* **2015**, *15*, 1603.
[39] S. G. Motti, M. Gandini, A. J. Barker, J. M. Ball, A. R. Srimath Kandada, A. Petrozza, *ACS Energy Lett.* **2016**, *1*, 726.
[40] H. Yuan, E. Debroye, G. Caliandro, K. P. F. Janssen, J. van Loon, C. E. A. Kirschhock, J. A. Martens, J. Hofkens, M. B. J. Roeffaers, *ACS Omega* **2016**, *1*, 148.
[41] W. Nie, J.-C. Blancon, A. J. Neukirch, K. Appavoo, H. Tsai, M. Chhowalla, M. A. Alam, M. Y. Sfeir, C. Katan, J. Even, S. Tretiak, J. J. Crochet, G. Gupta, A. D. Mohite, *Nat. Commun.* **2016**, *7*, 11574.
[42] N. Aristidou, C. Eames, I. Sanchez-Molina, X. Bu, J. Kosco, M. S. Islam, S. A. Haque, *Nat. Commun.* **2017**, *8*, 15218.
[43] C. Eames, J. M. Frost, P. R. F. Barnes, B. C. O'Regan, A. Walsh, M. S. Islam, *Nat. Commun.* **2015**, *6*, 7497.
[44] W. Nie, H. Tsai, R. Asadpour, J.-C. Blancon, A. J. Neukirch, G. Gupta, J. J. Crochet, M. Chhowalla, S. Tretiak, M. A. Alam, H.-L. Wang, A. D. Mohite, *Science* **2015**, *347*, 522.
[45] H. Tsai, W. Nie, J.-C. Blancon, C. C. Stoumpos, R. Asadpour, B. Harutyunyan, A. J. Neukirch, R. Verduzco, J. J. Crochet, S. Tretiak, L. Pedesseau, J. Even, M. A. Alam, G. Gupta, J. Lou, P. M. Ajayan, M. J. Bedzyk, M. G. Kanatzidis, A. D. Mohite, *Nature* **2016**, *536*, 312.
[46] M. I. Saidaminov, A. L. Abdelhady, B. Murali, E. Alarousu, V. M. Burlakov, W. Peng, I. Dursun, L. Wang, Y. He, G. Maculan, A. Goriely, T. Wu, O. F. Mohammed, O. M. Bakr, *Nat. Commun.* **2015**, *6*, 7586.
[47] O. D. Miller, E. Yablonovitch, S. R. Kurtz, *IEEE J. Photovoltaics* **2012**, *2*, 303.
[48] O. Durand, D. Rogers, F. H. Teherani, M. Andrieux, M. Modreanu, *Thin Solid Films* **2007**, *515*, 6360.
[49] N. C. Halder, C. N. J. Wagner, *Acta Crystallogr.* **1966**, *20*, 312.
[50] J. A. Venables, G. D. T. Spiller, M. Hanbucken, *Rep. Prog. Phys.* **1984**, *47*, 399.
[51] D. E. Wolf, J. Villain, *EPL* **1990**, *13*, 389.
[52] C. Bi, Q. Wang, Y. Shao, Y. Yuan, Z. Xiao, J. Huang, *Nat. Commun.* **2015**, *6*, 7747.
[53] M. D. Irwin, D. B. Buchholz, A. W. Hains, R. P. H. Chang, T. J. Marks, *Proc. Natl. Acad. Sci. USA* **2008**, *105*, 2783.
[54] C.-C. Chueh, C.-Z. Li, A. K. Y. Jen, *Energy Environ. Sci.* **2015**, *8*, 1160.
[55] J.-C. Blancon, W. Nie, A. J. Neukirch, G. Gupta, S. Tretiak, L. Cognet, A. D. Mohite, J. J. Crochet, *Adv. Funct. Mater.* **2016**, *26*, 4283.
[56] H. Tsai, W. Nie, Y.-H. Lin, J. C. Blancon, S. Tretiak, J. Even, G. Gupta, P. M. Ajayan, A. D. Mohite, *Adv. Energy Mater.* **2017**, *7*, 1602159.
[57] U. S. Joshi, Y. Matsumoto, K. Itaka, M. Sumiya, H. Koinuma, *Appl. Surf. Sci.* **2006**, *252*, 2524.
[58] W.-L. Jang, Y.-M. Lu, W.-S. Hwang, W.-C. Chen, *J. Eur. Ceram. Soc.* **2010**, *30*, 503.
[59] K. M. Knesting, H. Ju, C. W. Schlenker, A. J. Giordano, A. Garcia, O. N. L. Smith, D. C. Olson, S. R. Marder, D. S. Ginger, *J. Phys. Chem. Lett.* **2013**, *4*, 4038.
[60] Z. Tachan, I. Hod, M. Shalom, L. Grinis, A. Zaban, *Phys. Chem. Chem. Phys.* **2013**, *15*, 3841.
[61] R. A. Street, *Phys. Rev. B* **2011**, *84*, 075208.
[62] A. Maurano, R. Hamilton, C. G. Shuttle, A. M. Ballantyne, J. Nelson, B. O'Regan, W. Zhang, I. McCulloch, H. Azimi, M. Morana, C. J. Brabec, J. R. Durrant, *Adv. Mater.* **2010**, *22*, 4987.
[63] S. Shao, M. Abdu-Aguye, L. Qiu, L.-H. Lai, J. Liu, S. Adjokatse, F. Jahani, M. E. Kamminga, G. H. ten Brink, T. T. M. Palstra, B. J. Kooi, J. C. Hummelen, M. Antonietta Loi, *Energy Environ. Sci.* **2016**, *9*, 2444.
[64] A. J. Neukirch, W. Nie, J.-C. Blancon, K. Appavoo, H. Tsai, M. Y. Sfeir, C. Katan, L. Pedesseau, J. Even, J. J. Crochet, G. Gupta, A. D. Mohite, S. Tretiak, *Nano Lett.* **2016**, *16*, 3809.